Acousto-Electric Measurements on Graphene Transferred to YX128°-$LiNbO_3$ at 2.5 GHz

Mario Costanza[1], Léa La Spina[1], Arthur De Sousa[1], Djaffar Belharet[1], Ausrine Bartasyte[1,2] and Samuel Margueron[1]

[1] FEMTO-ST Institute, University of Bourgogne-Franche-Comte, CNRS UMR6174, Besancon, 25030, France
[2] Institut universitaire de France (IUF)

E-mail: xxx@xxx.xx

Received xxxxxx
Accepted for publication xxxxxx
Published xxxxxx

Abstract

Surface acoustic wave delay lines at about 2.5 GHz have been designed to measure the acousto-electronic transport of carriers in graphene transferred to piezoelectric substrate of YX128°-$LiNbO_3$. The process shows that monolayers of graphene on $LiNbO_3$ presents sheet resistances in the range of 733 to 1230 Ω/□ and ohmic contact resistance with gold of 1880 to 5200 Ωμm. The measurements with different interaction's lengths on graphene bars allows to extract carriers absorption and mobility from acousto-electric current. Graphene presents higher acousto-electronic interaction in the GHz range than previously reported values in the hundred of MHz range with carrier absorption losses of 109 m^{-1} and a mobility for acoustically generated charges in the order of 101 cm^2/Vs.

Keywords: micro-acoustic, graphene, acousto-electronic

1. Introduction

The development of microacoustic technologies had allowed major breakthroughs both in the miniaturization and performances of analog filters in the radiofrequency and microwave regimes [1,2]. Passive microacoustic filters are at the heart of high-end communication technologies, however several attempts have been dedicated in the developement of nonreciprocal and nonlinear microacoustic devices in order to enable more complex and performant architectures. The Acousto-Electric (AE) effect is the generation of a DC electric current from the propagation of an acoustic wave. This phenomenon is present in piezoelectric semiconductors like CdS [3–5], ZnO [5], GaN [6], or on heterostructures like AlGaAs/GaAS [7,8]. The indirect AE effect is used in AE amplifiers, which are nonreciprocal devices that can perform both amplification or reduction of acoustic waves by applying a DC bias on an a piezoelectric semiconductor or on a semiconductor [9], the gain applied on the acoustic field depends on the majoritary charge carriers and on direction of the current relatively to the acoustic field. Acoustic convolvers can achieve analog signal convolution through nonlinear interaction between two contra-propagating waves under a conductive medium [1,10], which can be a metallic film [11], or a semiconductive film [12]. However, performances on such devices is restricted by phenomena of mass loading and, in particular, convolvers devices are limited to the hundreds of MHz [1,10]. To improve the performance of such devices, it is necessary to use materials that would achieve higher AE coupling and lower power loss, while also providing high charge mobility. Since its discovery, some reports have been devoted to the measurements of AE effect in graphene up to 1 GHz [13–17]. As graphene is not piezoelectric, different heterostructures have been developed with direct excitation on

graphitized SiC [17] on graphene transferred of graphene to $LiNbO_3$ [14,15,17–20] or flip-chip of graphene on Si/SiO_2 on $LiNbO_3$ [21]. Indeed, graphene is an appealing material for AE coupling and the manipulation of electronic charges by acoustic waves. The low mass density of graphene disturbs only slightly the mass loading of micro-acoustic waves on piezoelectric substrates [22]. Moreover, graphene possesses a high charge carrier mobility which allows high frequency operations. Even if the control of the electrical properties of 2D materials, along with the electrical contacts, remains challeging [23], its resistivity can be tuned either electrically or through processing in order to optimize the coupling. For instance, Malocha et al. have recently demonstrated that graphene is a good candidate for energy coupling devices and AE SAW amplifiers on $LiNbO_3$ piezoelectric architectures [24,25]. Their works in operational frequency at 145 and 933 MHz respectively evaluate the technological interest for graphene. Moreover, They successed to tune the resistivity from 975 to 1500 Ω/□ through gate/oxide structure on a piezoelectric substrate. However, the potential interest of graphene for AE relies in its potential for ultra-high working frequency. Analog convolver would make a breakthrough if its performances would exceed greatly the one achieved by digital processing. This work focus then on the micro-fabrication process for the production graphene on $LiNbO_3$ devices, with 2.5 GHz SAW delay lines. A measurement of AE current and SAW propagation losses is done and compare with previous measurements of AE current.

2. Microfabrication

Black $LiNbO_3$ substrates YX-128° (rotation of the Y axis by 128° around X, and wave propagation along X) were diced in sizes of 20 mm x 22 mm, cleaned in acetone, sulfochromic acid and de-ionized (DI) water. The Figure 1 gives the flowchart for microacoustic fabrication and the tranfer of graphene. The first step consists in the microfabrication of the interdigit SAW transducers and charge-collecting electrodes for graphene. A positive resist, ARP 6200.09, is spined coated for a thickness of 288 nm and bakes in oven for 30 minutes at 150°C. It is then followed by a spin-coat of an Electra conductive resist. The IDTs are therefore patterned through electron-beam lithography with a minimum feature size is of ~300 nm. The Electra resist is then removed in DI-water and ARP 6200.09 is developed in a solution of Amyl-acetate and MIBK:Iso-Propyl Alcohol (IPA) (1:3) for 30 s. The surface is treated for 5 s in O_2 plasma just before the deposition of the Ti (10 nm)/Au (30 nm) through e-beam evaporation. The sample is then lift off in NF26A. The sample is then cleaned in acetone, IPA and DI water. In a second step, the transfer of graphene was carried out using a transfer kit of a 10 x 10 mm graphene sheet on a water-soluble polymer from Graphenea Foundry (Spain) [26]. Step 3 describes the patterning process of the graphene. A protecting positive S1813 photoresist is spined coated and impressed through ultraviolet (UV) lithography (EVG 680). The step 4 consists in the removal of unprotected graphene by an oxygen plasma etching for 30 s, the photoresist is then removed by the remover solution 1165, and rinced in IPA and DI water. The contact pads are made in step 5, the photoresist AZNLOF 2000 is spin-coated, baked for 3 minutes in oven at 110°C and then patterned through UV lithography. Deposition of Ti (10 nm)/Au (200 nm) is then achieved through sputtering and the lift-off is done in the 1165 remover solution. The samples are then cleaned in acteone, IPA and DI water. In step 6, annealing is performed to improve both the resistivity of the graphene and the graphene-metal electrical contacts, this is done in a tube furnace with an argon atmosphere at the temperature of 120°C for 90 minutes. This step was critical because temperatures greater than 150°C, which is lower than annealing temperatures used for graphene on silicon wafers, had shown the disapperance of graphene. Raman spectra and a mapping of graphene on a $LiNbO_3$ has been acquired in backscattering geometry with unpolarized scattering at 532 nm excitation (Monovista, S&I). The time acquisition was 20 s by spectra with a power 10 mW and 100X objective. Figure 2.b illustrates a mapping of 50 x 50 µm made of 25 x 25 points.

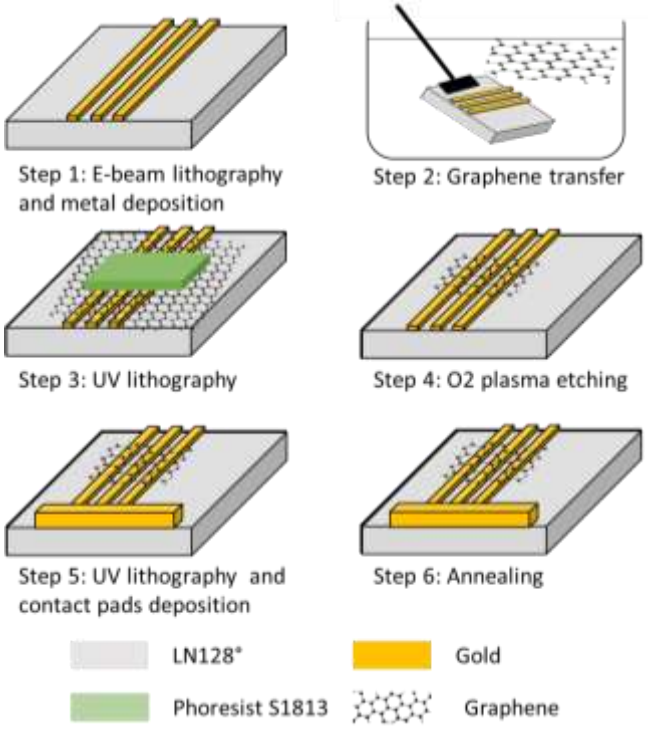

Figure 1: flowchart steps for graphene transfer.

Electrical characterization of ohmic contact and sheet resistance has been measured by Transmission Line Model (TLM) method [27]. The resistive measures were performed through the 4-point probes method, and a Keithley 6221 current source and a Keithley 6182 nano-voltmeter were used. In order to limit temperature changes due to power dissipation,

the current source was set to generate short pulses at ±50 nA, and the voltage measures were taken after the transitory effects. The resistance was measured for different distances and is reported in Figure 3. Finally, Figure 4 shows the set-up for the AE measurements. It is composed of a 100 kHz to 6 GHz high power signal generator (Keysight N5181B), connected through port 1 to the IDT 1, and the AE current is measured though a Source Measurement Unit (Keithly 2636B), isolated from the High-Frequency component by a 6 GHz bias-tee (ZFBT-6G+) connected to port 2, which is then connected to pads 1-10. For the measure of the scattering parameters, a Vector Network Analyzer (VNA Keysight P5004) was used, connecting port 1 to IDT 1 and port 2 to IDT 2.

2. Results

The analysis of the homogeneity of the processed devices has been performed by means of an optical microscope. As the visibility of graphene on $LiNbO_3$ is quite low (few percent of contrast), more precise measures have been carried out through Raman spectroscopy [28–30]. The Raman spectra has been fitted using pseudo-voigt profiles to plot the 2D and G intensities ratio. Figure 2.a represents a typical raman scan of graphene on $LiNbO_3$ after processing and Figure 2.b presents a typical mapping. The 2D/G ratio stays firmly above ~3.3, and steeply decreases where it the graphene had been etched away. This confirms that the transferred graphene is monolayer [28], and uniform on all our devices. No imperfections such as holes or foldings of the graphene sheet has been observed. The only possible problem occours out of the cleanroom with dust contamination and necessitate a cleaning with acetone. In order to further confirm the high quality of graphene, the DC resistivity values have been analysed through the TLM method in which a bar of graphene is contacted in multiple differently spaced points. The chart in Figure 3 represents the data gathered from a TLM device of an 80 µm-wide device and distances from 10 to 135 µm long, the measures have been carried in air at 25°C. The resistivity of graphene and the contact resistance shown are extracted from the fitting [31–33]. The intercept on the resistance axis is the total contact resistance, which is equal to:

$$R_{tot} = 2 \cdot R_m + 2 \cdot R_i \qquad \textit{(Eq. 1)}$$

Where the factor 2 is from the fact graphene is from the two contact points, R_m is the resistance of the gold contact, and R_i is the resistance of the graphene-metal interface. The value of the contact resistivity is therefore found by multiplying the interface resistance by the width of the interface. The resistivity of the graphene is found by multiplying the slope of the curve, which is the line resistivity in Ω/µm, with the width of the TLM device. The resistivity of the graphene has been found to be 733.4 Ω/□ and, measuring a resistance for the gold contacts of ~21 Ω. The contact resistivity between the graphene and gold is 1880 Ωµm. Further measures on other TLM devices revealed that the resistivity values can vary considerably on the same sample, and have been found to be in the range of 733-1230 Ω/□ and 1880-5200 Ωµm for the graphene's sheet resistivity and contact resistivity respectively.

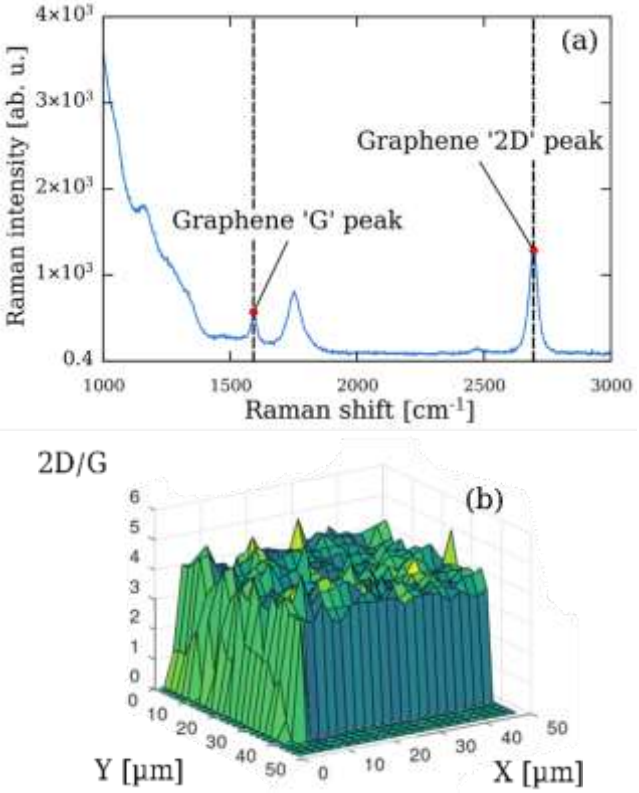

Figure 2: Typical Raman spectrum of graphene transferred to $LiNbO_3$ (a) and mapping of 2D/G ratio on a 50 µm x 50 µm area (b).

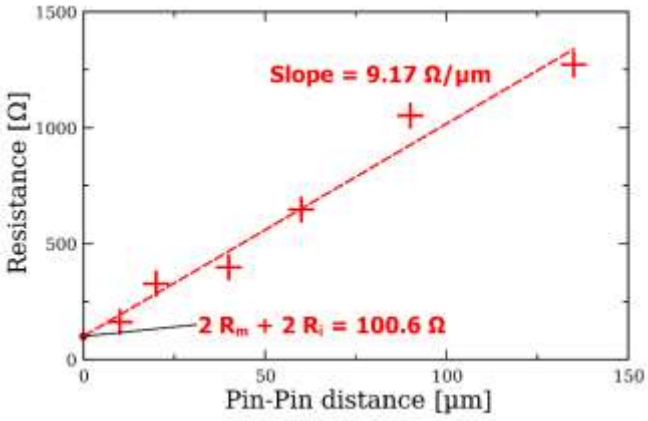

Figure 3: TLM plot for a 80 µm-wide graphene device with electrical gold contacts.

The AE current measurements have been performed with the set-up represented in Figure 4 and the device schematic of Figure 5. The SAW delay line consists of 14 pairs of IDT with

an aperture of 80 µm and a periodicity of 1.35 µm, each digit having a width of 288 nm. The distance beween IDT 1 and IDT 2 is 2 mm.

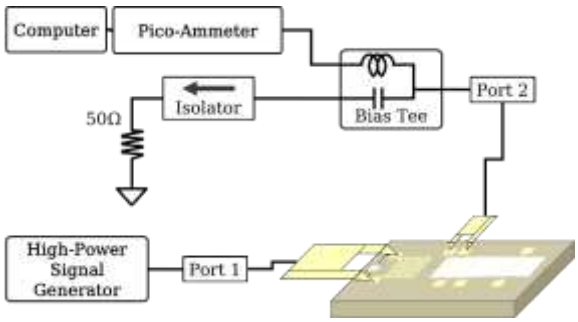

Figure 4: Representation of the setup for the AE current measurements.

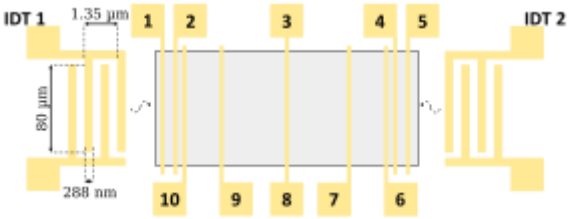

Figure 5: Representation of a device used for AE current characterization.

The device with graphene has been contacted physically through GS probes on IDT 1 and 2 with wave impedance of 50 Ω, and measurements of the scattering parameters S_{11} and S_{21} have been taken in the frequency range between 1 GHz and 4 GHz with VNA. The results are represented in Figure 6.a and Figure 6.b respectively. The scattering parameters of the SAW delay line confirmed a first order resonance around 2.5 GHz, but, with an insertion loss of value 30 dB. This small value could be due impedance mismatch and propagation losses. The total lost power, relative from IDT1 as imput, has been computed from the scattering parameters as:

$$\frac{P_{lost}}{P_{in,1}} = \frac{|a_1|^2 - |b_1|^2 - |b_2|^2}{|a_1|^2} = 1 - |S_{11}|^2 - |S_{22}|^2 \quad \textit{(Eq. 2)}$$

where a_1, b_1 and b_2 are the Kurokawa wave parameters for the input electromagnetic wave at port 1 and output electromagnetic wave at ports 1 and 2 respectively [34]. The resulting data for the power lost is plotted on Figure 6.c and shows that a considerable portion of the acoustic power is lost during transmission. This could be due to the long delay line (2 mm) and high frequency losses of the acoustic wave. Further characterization of other delay lines devices, with or without graphene, yielded similar results, with the center frequency usually being between 2.2 GHz and 2.7 GHz.

The acquired AE currents on graphene with different pins are presented in Figure 7.a in linear scale and Figure 7.b in logarithmic scale. The acoustic current has been generated through a high-power signal generator connected directly on an IDT and the AE current has been measured by means of an ammeter, connected to a probe placed on adjacent pads.

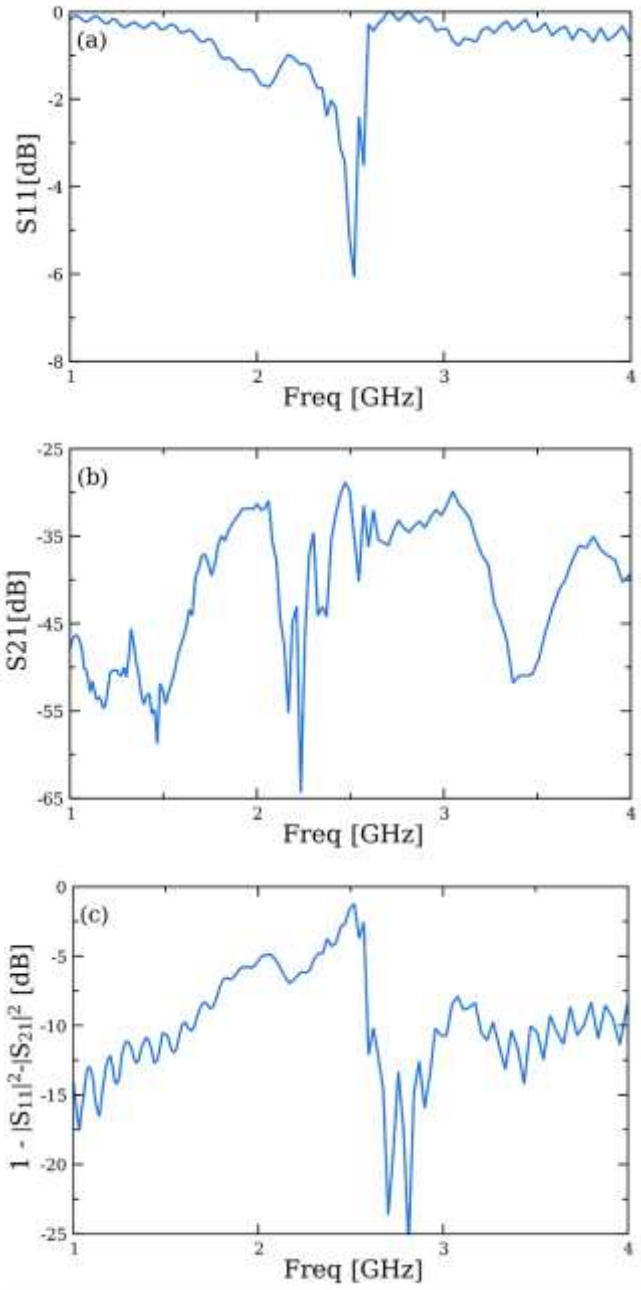

Figure 6: Characterization of the S11 (a), S21 (b) and dissipated power (c) vs input frequency on graphene transferred to $LiNbO_3$ between IDT 1 and 2.

In order to shield the ammeter from the microwave electromagnetic field component, both for protection of the instrumentation and for better accuracy, the probe was first connected by a bias-tee whose RF branch was connected to an isolator and a load of 50 Ω, while the DC branch was connected to the ammeter (Figure 4), the AE current collected have been therefore logged. During each measurement for the

AE current the generator has first been set up to generate a signal at 2.5 GHz with low amplitude (0 dBm), the frequency has then been slowly tuned manually while the AE current was monitored. The frequency that maximize the current value was found at2.507 GHz, which was in line to what expected from Figure 5.a and Figure 5.b. Once the central frequency was found, the power has been gradually increased up to 0.3 W. Afterwards the same power sweep has been also repeated for the other data points. The central frequency did not show a signicant shift with excitation power and we can neglect dissipation and temperature effects.

3. Discussion

The current for a short-circuited AE current loop for hybrid piezoelectric-2D electron systems in the case of no-magnetic fields [7,8,35] is described by the following equation:

$$\mathrm{I_{AE}} = \mu \cdot P \cdot \Gamma / v$$

(Eq. 3)

where μ is the carrier mobility, P is the acoustic power, Γ is the attenuation coefficient for the acoustic field due to the interaction with the charge carriers, and v is the speed of the surface wave. For a 2D electron system on piezoelectric, assuming a simple relaxation model for the SAW-charge carriers interactions, the value of Γ can be found as [7]:

$$\Gamma = k \cdot \frac{{K_{eff}}^2}{2} \cdot \frac{\rho_M/\rho_\square}{1 + (\rho_M/\rho_\square)^2}$$

(Eq. 4)

where k is the SAW's wavenumber, ${K_{eff}}^2$ is the effective piezoelectric coupling factor, and it's equal to 0.056 for $LiNbO_3$ with cut YX128°, $\rho_\square$ is the surface resistivity and ρ_M is a constant, equal to approximatey 800 kΩ for $LiNbO_3$ with cut YX128°. In order to correctly evaluate the power inside Eq. 3, it is necessary to estimate the different contributions to the decrease in the amplitude of the acoustic field from the IDTs to the graphene. The power at the graphene interface can be calculated as:

$$P = \eta_{IDT} \cdot \eta_P \cdot P_{in} \cdot e^{-2\alpha \cdot \Delta x}$$

(Eq. 5)

where P_{in} is the input electrical power, η_{IDT} is the conversion efficiency between the electrical signal at the IDT and acoustic power in the delay line, the efficiency η_P is a factor to which accounts for the power loss due to the cables, probes and various connectors, Δx is the distance between the IDT and the first pad on the graphene, and α represents the losses of the acoustic field due to damping. If assuming that the ohmic losses are negligible, all of the input electric power is either reflected back or converted to SAW:

$$P_{in} = |a_1|^2 = |b_1|^2 + 2 \cdot P_A$$

(Eq. 6)

where P_A is the acoustic power generated at one side of the IDT and the factor 2 derives from the a-directionality of our IDT design, meaning the electrical power is split equally between both the left and right side. From Eq. 6, the value of the η_{IDT} can be found from the scattering parameter S_{11} as:

$$\eta_{IDT} = \frac{P_A}{|a_1|^2} = \frac{1 - |S_{11}|^2}{2}$$

(Eq. 7)

At resonance, the $|S_{11}|$ = -6 dB, which implies η_{IDT} = 0.37. The value of η_P was measured experimentally and the value found is η_P ~ 0.83 for both port 1 and port 2. As for α, it can be found from S_{11} and S_{21} by rewriting Eq. 6 in terms of the electric wave in port 2 instead of the acoustic power at port 1:

$$|a_1|^2 = |b_1|^2 + 2 \cdot e^{2\alpha \cdot L} \cdot \frac{|b_2|^2}{\eta_{IDT}\eta_P}$$

(Eq. 8)

where L is the length of the delay line and $|b_2|^2/\eta_{IDT}\eta_P$ is the amplitude of the acoustic wave on IDT 2. Finally, Eq. 8 can be manipulated in order to find:

$$\alpha = \frac{1}{2 \cdot L} \cdot log\left(\frac{1 - |S_{11}|^2}{2 \cdot |S_{21}|^2} \cdot \eta_{IDT} \cdot \eta_P\right)$$

(Eq. 9)

By performing a characterization on a delay line without graphene, it was found α = 1550 m^{-1}, which means that the acoustic wave, when it reaches the graphene is reduced by a factor of ~0.053. Different sets of AE current measures have been performed, in each the ammetter was used to measure the acoustic current between the pads 1-2, 2-3, 10-9 and 9-8, each couple of pad has a distance between each other of 14.5 µm, 414 µm, 40.5 µm and 344.3 µm respectively. The data collected are represented in Figure 8. The AE current is always positively signed with respect to the propagating direction of the acoustic field, implying the majoritary charges carriers are holes, due to the p-doping in the graphene caused from the adsorption of gases like O_2 and H_2O [30]. For each plot, accordingly with the Eq. 3, AE current varies linearly with the input power, and the maximum reached values lie at 4.5 µA, 188 nA, 950 nA and 68 nA respectively. However, the current values present a significative variation from a plot to the next, such that the maximum current measured from the pads 1-2 is ~4.7 times higher than what measured on pads 10-9, and ~66.2 times higher than for pads 9-8. This effect could be due to the previously discussed power losses on the delay line itself. As a way to check this hypothesis, the amplitude the amplitude of the AE current at 0.3 W of input power, has been plot with respect to the average distance to the first contact pad, as shown in Figure 8, showing an exponential decrease with the distance. By using Eq. 3 and Eq. 4, it is possible to find the values of the loss factor Γ and charge mobility from the data acquired. The values found are of Γ = 109 m^{-1} and μ = 101 cm^2/Vs for a measured graphene resistivity for the AE device of ~800 Ω/□.

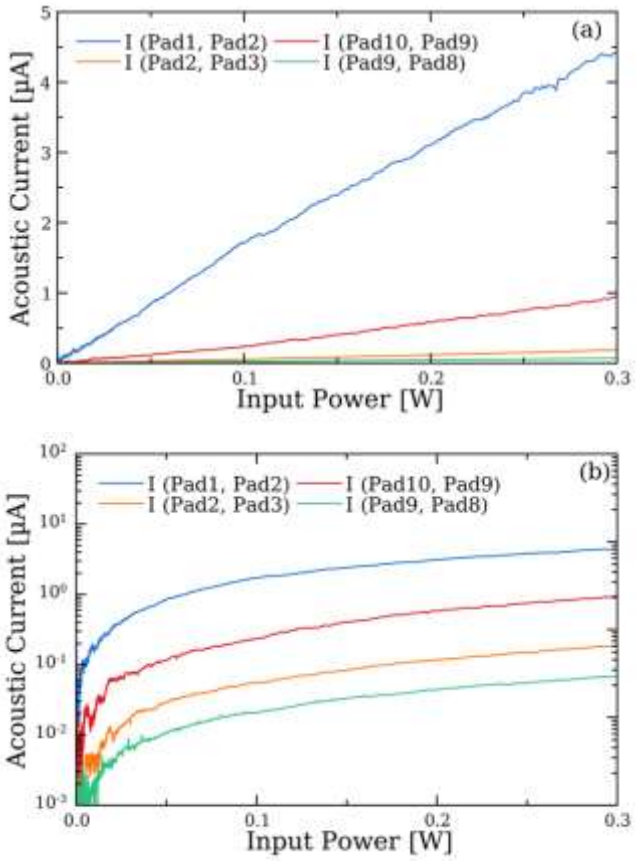

Figure 7: AE current measurements in linear scale (a), and in logarithmic scale (b).

Table 1 reports a comparison of AE parameters of graphene transferred on $LiNbO_3$ in the range of 11 MHz to 2.5 GHz. The graphene DC resistivity varies from 0.8 kΩ/□ in air to 154 kΩ/□ in vaccum. Considering only values in air, the resistivity varies from 0.8 to 4.8 kΩ/□ in line with CVD graphene properties transferred on Si/SiO_2 [36]. The DC mobility of our graphene is expected to be of the order of 1500 cm^2/Vs as on Si/SiO_2 for a similar resistivity [15,24,26]. Meanwhile, the acousto-electronic mobility measured in table 1 differs significantly from DC mobility. It is comprised between 68 and 109 cm^2/Vs for low resistivity graphene and from 5 to15 cm^2/Vs in higly resistive graphene. The mobility of Equation 3 and Equation 4 is then not the DC mobility. We present four possible reasons for the discrepancies between the theoretical values and the results. One of the main reason is that the mobility in AE is due to the inhomogeneous electric field (over the acoustic wavelength in the range of microns) and transverse electric field accompagning the acoustic wave, as for DC mobility it is measured with an electric field longitudinal to the plane of graphene. A second reason for this decrepancy is that, as compared to others piezoelectric semiconductors where little difference was observed on mobility (for instance 2DEG GaAs [35]), the amplitude of the electric field in the graphene may differ from the one within the piezoelectric. Indeed, a dead layer forms on the ferroelectric surface of $LiNbO_3$ which may attenuate the amplitude of the electric field at the extreme surface of the graphene [37].

A third reason is based on the the difference of the mobility we measure at 2.5 GHz of 109 cm^2/Vs with the one extracted from the data by *Miseikis et al.* at 110 MHz [13] of 68 cm^2/Vs. As both paper consider CVD graphene transferred to $LiNbO_3$ [38], one can consider a dependance on the wavelength of acoustic field of respectively 30 µ and 1.6 µm. However, this result doesn't follow *Venugopal et al.* [39] report. Indeed, a significant decrease of mobility was observed for transport distances less than ~5 µm due to a switch in prevelent charge transport mechanism from quasi-ballistic to diffusive. In our case, the highest mobility is found with wavelength of the order of 1.6 µm wich is much smaller that the critical distance found at around 5 µm. In this case, the higher resistance of *Miseikis et al.* due to defects and scattering of carriers may explain their lower mobility. Finally, a fourth hypothesis is that in Equations 5 to 9, we explicitely separate the acoustic losses in the $LiNbO_3$ substrate from the losses in graphene. We then found lower losses factor Γ for similar power. As a consequence, the mobility factor is increase in proportion than if we would have considered the acoustic losses. In this matter, very little information has been previously reported in papers of Table 1. From the previous discussion, a high uncertainty exist in defining the AE mobility from the to DC mobility. The extracted AE mobility shows values much higher than other reported values, indicating a better AE coupling of in GHz range. As a consequences, the same claims on the coupling factor K_{eff}, and therefore the factor Γ at extrême surface.

Still, the generic equation 3 and 4 have been verified but little attention has been paid to the actual values. This indicates that there is still experiemental and theoretical work to pursue in this direction.

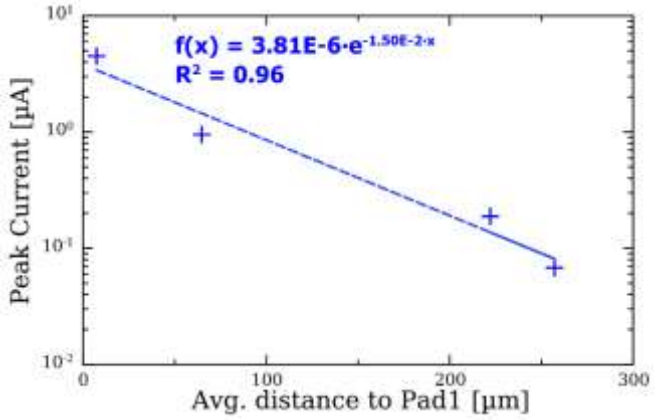

Figure 8: Acoustic current at 0.3 W, 2.507 GHz vs average distance from Pad 1.

Table 1: Values of Γ and μ measured on YX128°-$LiNbO_3$ at room temperature with the frequency and the typical feature size of the devices (are values computed from data, - is for data not available).*

Ref.	ρ [kΩ/□]	Γ [m^{-1}]	μ_{AE} [cm^2/Vs]	$\Gamma \cdot \mu_{AE}$	Size [µm]	Freq. [MHz]
[13]	4.8	29*	68*	2001*	30	110
[16]	154 (vac.)	2910*	8	23280	200, 300, 500	11,32, 97,18, 356
[15]	77* (vac.)	1100	15	16500	300	11,32, 269
[14]	-	150	5	750	29	332
[24, 25]	0.9-1.5 (gate)	-	-	-	127	331
our	0.8	109	101	12000	14, 40, 344	2500

3. Conclusion

Surface Acoustic wave delay lines at about 2.5 GHz carriers have been deisigned to measure acousto-electronic transport of graphene. Even if the insertion loss of our device remains quite high due to the unoptimized impedance matching at 50 Ω and wave damping on $LiNbO_3$, the results show that graphene presents a very strong acousto-electronic interaction in the GHz range.

Acknowledgements

This work was supported by the French RENATECH network and its FEMTO-ST technological facility, the french national ANR under contract MAXSAW and the graduate school EUR EIPHI for their finacial support through IGRF project.

References

[1] Colin Campbell 1989 *Surface Acoustic Wave Devices and Their Signal Processing Applications* (Academic Press Inc.)

[2] Campbell C K 1989 Applications of surface acoustic and shallow bulk acoustic wave devices *Proc. IEEE* **77** 1453–84

[3] Das P and Araghi M N 1972 Surface Wave Signal Processor Using CdS-Fluid-LiNbO3 Structure *1972 Ultrasonics Symposium* 1972 Ultrasonics Symposium (IEEE) pp 306–9

[4] Hutson A R, McFee J H and White D L 1961 Ultrasonic Amplification in CdS *Phys. Rev. Lett.* **7** 237–9

[5] Hutson A R 1961 Piezoelectric Scattering and Phonon Drag in ZnO and CdS *J. Appl. Phys.* **32** 2287–92

[6] Gokhale V J, Shim Y and Rais-Zadeh M 2010 Observation of the acoustoelectric effect in gallium nitride micromechanical bulk acoustic filters *2010 IEEE International Frequency Control Symposium* 2010 IEEE International Frequency Control Symposium (FCS) (Newport Beach, CA, USA: IEEE) pp 524–9

[7] Wixforth A, Scriba J, Wassermeier M, Kotthaus J P, Weimann, G, and Schlapp, W 1989 Surface acoustic waves on GaAs/Al x Ga 1− x As heterostructures *Phys. Rev. B* **40** 7874

[8] Shilton J M, Mace D R, Talyanskii V I, Simmons M Y, Pepper M, Churchill A C and Ritchie D A 1995 Experimental study of the acoustoelectric effects in GaAs-AlGaAs heterostructures *J. Phys. Condens. Matter* **7** 7675–85

[9] Adler R 1971 Simple theory of acoustic amplification *IEEE Trans. Sonics Ultrason.* **18** 115–8

[10] Morgan D P 2007 *Surface acoustic wave filters: with applications to electronic communications and signal processing* (Amsterdam ; London: Academic Press)

[11] Defranould P and Maerfeld C 1976 A SAW planar piezoelectric convolver *Proc. IEEE* **64** 748–51

[12] Reible S A 1981 Acoustoelectric Convolver Technology for Spread-Spectrum Communications *IEEE Trans. Microw. Theory Tech.* **29** 463–74

[13] Miseikis V, Cunningham J E, Saeed K, O'Rorke R and Davies A G 2012 Acoustically induced current flow in graphene *Appl. Phys. Lett.* **100** 133105

[14] Bandhu L and Nash G R Controlling the properties of surface acoustic waves using graphene *Nano Res* 7

[15] Bandhu L and Nash G R 2014 Temperature dependence of the acoustoelectric current in graphene *Appl. Phys. Lett.* **105** 263106

[16] Bandhu L, Lawton L M and Nash G R 2014 Macroscopic acoustoelectric charge transport in graphene *Appl Phys Lett* 5

[17] Hernández-Mínguez A, Tahraoui A, Lopes J M J and Santos P V 2016 Acoustoelectric transport at gigahertz frequencies in coated epitaxial graphene *Appl. Phys. Lett.* **108** 193502

[18] Poole T and Nash G R 2017 Acoustoelectric Current in Graphene Nanoribbons *Sci. Rep.* **7** 1767

[19] Nunes O A C 2014 Piezoelectric surface acoustical phonon amplification in graphene on a GaAs substrate *J. Appl. Phys.* **115** 233715

[20] Okuda S, Ikuta T, Kanai Y, Ono T, Ogawa S, Fujisawa D, Shimatani M, Inoue K, Maehashi K and Matsumoto K 2016 Acoustic carrier transportation induced by surface acoustic waves in graphene in solution *Appl. Phys. Express* **9** 045104

[21] Lane J R, Zhang L, Khasawneh M A, Zhou B N, Henriksen E A and Pollanen J 2018 Flip-chip gate-tunable acoustoelectric effect in graphene *J. Appl. Phys.* **124** 194302

[22] Hernández-Mínguez A, Liou Y-T and Santos P V 2018 Interaction of surface acoustic waves with electronic excitations in graphene *J. Phys. Appl. Phys.* **51** 383001

[23] Giubileo F and Di Bartolomeo A 2017 The role of contact resistance in graphene field-effect devices *Prog. Surf. Sci.* **92** 143–75

[24] Malocha D C, Carmichael C and Weeks A 2020 Acoustoelectric Amplifier With 1.2-dB Insertion Gain Monolithic Graphene Construction and Continuous Wave Operation *IEEE Trans. Ultrason. Ferroelectr. Freq. Control* **67** 1960–3

[25] Carmichael C, Malocha D C and Weeks A 2019 Asymmetric energy coupling through acoustoelectric effect using graphene on lithium niobite surface acoustic wave delay line in GHz Range *2019 IEEE International Ultrasonics Symposium (IUS)* 2019 IEEE International Ultrasonics Symposium (IUS) (Glasgow, United Kingdom: IEEE) pp 702–5

[26] Graphenea, Inc. Graphenea Monolayer Graphene on Polymer Film Datasheet

[27] Reeves G K and Harrison H B 1982 Obtaining the specific contact resistance from transmission line model measurements *IEEE Electron Device Lett.* **3** 111–3

[28] Kumar V, Kumar A, Lee D-J and Park S-S 2021 Estimation of Number of Graphene Layers Using Different Methods: A Focused Review *Materials* **14** 4590

[29] Ferrari A C and Basko D M 2013 Raman spectroscopy as a versatile tool for studying the properties of graphene *Nat. Nanotechnol.* **8** 235–46

[30] Ni Z H, Wang H M, Luo Z Q, Wang Y Y, Yu T, Wu Y H and Shen Z X 2010 The effect of vacuum annealing on graphene *J. Raman Spectrosc.* **41** 479–83

[31] Hsu A, Wang H, Kim K K, Kong J and Palacios T 2011 Impact of Graphene Interface Quality on Contact Resistance and RF Device Performance *IEEE Electron Device Lett.* **32** 1008–10

[32] Moon J S, Antcliffe M, Seo H C, Curtis D, Lin S, Schmitz A, Milosavljevic I, Kiselev A A, Ross R S, Gaskill D K, Campbell P M, Fitch R C, Lee K-M and Asbeck P 2012 Ultra-low resistance ohmic contacts in graphene field effect transistors *Appl. Phys. Lett.* **100** 203512

[33] Zhong H, Zhang Z, Chen B, Xu H, Yu D, Huang L and Peng L 2015 Realization of low contact resistance close to theoretical limit in graphene transistors *Nano Res.* **8** 1669–79

[34] Kurokawa K 1965 Power Waves and the Scattering Matrix *IEEE Trans. Microw. Theory Tech.* **13** 194–202

[35] Rotter M, Wixforth A, Ruile W, Bernklau D and Riechert H 1998 Giant acoustoelectric effect in GaAs/LiNbO3 hybrids *Appl. Phys. Lett.* **73** 2128–30

[36] Zhang Y, Zhang L and Zhou C 2013 Review of Chemical Vapor Deposition of Graphene and Related Applications *Acc. Chem. Res.* **46** 2329–39

[37] Chang L-W, Alexe M, Scott J F and Gregg J M 2009 Settling the “Dead Layer” Debate in Nanoscale Capacitors *Adv. Mater.* **21** 4911–4

[38] De Fazio D, Purdie D G, Ott A K, Braeuninger-Weimer P, Khodkov T, Goossens S, Taniguchi T, Watanabe K, Livreri P, Koppens F H L, Hofmann S, Goykhman I, Ferrari A C and Lombardo A 2019 High-Mobility, Wet-Transferred Graphene Grown by Chemical Vapor Deposition *ACS Nano* **13** 8926–35

[39] Venugopal A, Chan J, Li X, Magnuson C W, Kirk W P, Colombo L, Ruoff R S and Vogel E M 2011 Effective mobility of single-layer graphene transistors as a function of channel dimensions *J. Appl. Phys.* **109** 104511

[40] Venica S, Driussi F, Gahoi A, Palestri P, Lemme, Max C and Selmi L 2018 On the Adequacy of the Transmission Line Model to Describe the Graphene–Metal Contact Resistance *IEEE Trans. Electron Devices* **65** 1589–96